This article has been accepted for inclusion in a future issue of this journal. Content is final as presented, with the exception of pagination.

Basis Pursuit Anisotropic Inversion Based on the L_1–L_2-Norm Regularization

Cong Luo, Jing Ba, José M. Carcione, and Qiang Guo

***Abstract*—Prestack seismic inversion for VTI media (transversely isotropic with vertical axis of symmetry) is a technique that can be useful to obtain the properties (velocity, density, and anisotropy parameters) of shale reservoirs. Since conventional inversion with smooth constraints (e.g., L_2-norm) is not appropriate, we propose a basis pursuit inversion (BPI) extended to VTI media, where: 1) we decompose the five elasticities into basis pursuit pairs by a dipole decomposition; 2) instead of the commonly used L_1-norm, the L_1–L_2 is implemented as a regularization constraint to achieve higher resolution and stability; and 3) alternating direction method of multipliers (ADMM) is used to obtain the solutions. Since the problem is highly ill-posed, we perform the inversion using PP and PS multicomponent seismic data. The examples (synthetic and real data) verify the higher resolution and better antinoise performance of the proposed method.**

***Index Terms*—Basis pursuit inversion (BPI), prestack seismic inversion, sparse constraint, transversely isotropic with vertical axis of symmetry (VTI) medium.**

I. Introduction

PRESTACK seismic inversion is one of the most effective geophysical techniques for reservoir characterization and fluid identification when applied to amplitude versus offset (AVO) and amplitude versus angle (AVA) [1]–[4]. The method is helpful to delineate lithological boundaries, structural features, and fluid distributions.

Stochastic inversions based on well-logs and geostatistical information achieve high vertical resolution [5], but are not free of uncertainties. On the other hand, multiscale inversion uses high-frequency components to increase the resolution [6], but these components are in many cases contaminated by noise, which inevitably affects the result. Moreover, Tikhonov regularization commonly used in conventional seismic inversion suffers from smooth and fuzzy edges in terms of vertical resolution [7]. Therefore, introducing sparse constraints or edge-preserving (EP) regularizations into prestack inversions has been an effective way to improve the resolution. Many regularizations have been implemented, namely, Cauchy [8], [9], Huber [10], total variation [11], [12], and Markov-random-field-based EP [7], [13], [14]. Zhang and Castagna [15] decomposed reflection coefficients into odd and even pairs and implemented the poststack basis pursuit inversion (BPI) by using the L_1-norm constraint to obtain sparse results. Due to its effectiveness in terms of sparsity, BPI has been extended to prestack BPI, which has been applied to thin-layer prediction and fluid identification [16]. These works are based on the assumption of an isotropic medium.

Nowadays, unconventional reservoirs [17], such as shale oil/gas, are increasingly attracting the attention of the industry. The transversely isotropic with vertical axis of symmetry (VTI) characteristics of these rocks (thin layers) preclude the use of isotropic inversion [18], 19]. Although the exact expressions of the reflection coefficients of VTI media are available [20]–[22], their complex form limits the applications. Simplified weak-anisotropy expressions [23] have been introduced into prestack inversion [19], [24]. The existing methods focus more on improving the estimation accuracy of the elasticities but not the resolution. However, high-resolution inversion results are crucial to the predication of such unconventional reservoirs where textured shales or horizontal thin layers are often contained.

We propose a prestack high-resolution inversion based on a BPI scheme for VTI media, where we introduce the L_1–L_2 sparser norm [25] as constraint. The regularized function is minimized with the alternating direction method of multipliers (ADMM) algorithm [26]. It is well-known that the inversion for VTI media is highly ill-posed, since five elastic constants need to be estimated. Therefore, we add PS wave data into the inversion to reduce multiple solutions and improve the accuracy.

II. Theory and Methodology

A. Forward Modeling for VTI Media

Let us consider the xy plane. The exact expressions of the reflection coefficients were given by Graebner [20] and Daley and Hron [27]. However, due to the highly nonlinear relationships between the reflection coefficients and the elasticities, these expressions are rarely used in prestack seismic inversion. Hence, many approximations have been derived and adopted in AVA inversion due to their simplicity. According to Rüger [23] and Lou and Ming [25], the PP and PS reflection coefficients are

$$R_{\mathrm{PP}} = R_{\mathrm{PP}}^{\mathrm{iso}} + R_{\mathrm{PP}}^{\mathrm{aniso}}, \quad R_{\mathrm{PS}} = R_{\mathrm{PS}}^{\mathrm{iso}} + R_{\mathrm{PS}}^{\mathrm{aniso}} \tag{1}$$

where $R_{\mathrm{PP}}^{\mathrm{iso}}$, $R_{\mathrm{PP}}^{\mathrm{aniso}}$, $R_{\mathrm{PS}}^{\mathrm{iso}}$, and $R_{\mathrm{PS}}^{\mathrm{aniso}}$ denote the isotropic and anisotropic terms, respectively

$$R_{\mathrm{PP}}^{\mathrm{iso}}(\theta) = A \cdot r_\alpha + B \cdot r_\beta + C \cdot r_\rho, \quad R_{\mathrm{PP}}^{\mathrm{aniso}}(\theta) = D \cdot r_\delta + E \cdot r_\varepsilon \tag{2}$$

and

$$R_{\mathrm{PS}}^{\mathrm{iso}}(\theta) = F \cdot r_\alpha + G \cdot r_\beta + H \cdot r_\rho, \quad R_{\mathrm{PS}}^{\mathrm{aniso}}(\theta) = H \cdot r_\delta + L \cdot r_\varepsilon \tag{3}$$

Manuscript received February 4, 2021; revised March 28, 2021; accepted April 16, 2021. This work was supported in part by the National Natural Science Foundation of China under Grant 42004111, in part by the China Postdoctoral Science Foundation under Grant 2019M661716, in part by the Fundamental Research Funds for the Central Universities of China under Grant B200202135, in part by the Natural Science Foundation of Zhejiang Province under Grant LQ21D040001, in part by the Jiangsu Innovation and Entrepreneurship Plan, and in part by the Jiangsu Province Science Fund for Distinguished Young Scholars under Grant BK20200021. *(Corresponding author: Jing Ba.)*

Cong Luo, Jing Ba, and Qiang Guo are with the Department of Geological Engineering, Hohai University, Nanjing 211100, China (e-mail: jba@hhu.edu.cn).

José M. Carcione is with the National Institute of Oceanography and Applied Geophysics (OGS), 34010 Trieste, Italy, and also with the Department of Geological Engineering, Hohai University, Nanjing 211100, China.

Color versions of one or more figures in this letter are available at https://doi.org/10.1109/LGRS.2021.3075062.

Digital Object Identifier 10.1109/LGRS.2021.3075062

1545-598X © 2021 IEEE. Personal use is permitted, but republication/redistribution requires IEEE permission.
See https://www.ieee.org/publications/rights/index.html for more information.

Authorized licensed use limited to: Konya Teknik Universitesi. Downloaded on May 25,2021 at 23:14:15 UTC from IEEE Xplore. Restrictions apply.

This article has been accepted for inclusion in a future issue of this journal. Content is final as presented, with the exception of pagination.

where

$$A = \frac{1}{2\cos^2\theta}, \quad B = -\frac{4\bar{\beta}^2}{\bar{\alpha}^2}\sin^2\theta, \;\; C = \frac{1}{2} - \frac{2\bar{\beta}^2}{\bar{\alpha}^2}\sin^2\theta \tag{4a}$$

$$D = \frac{1}{2}\sin^2\theta, \quad E = \frac{1}{2}\sin^2\theta\tan^2\theta \tag{4b}$$

$$F = 0, \quad G = -2\frac{\bar{\beta}}{\bar{\alpha}}\sin\theta\cos\theta + 2\left(\frac{\bar{\beta}}{\bar{\alpha}}\right)^2\frac{\sin^3\theta}{\cos j} \tag{4c}$$

$$H = -\frac{\sin\theta}{2\cos j} - \frac{\bar{\beta}}{\bar{\alpha}}\sin\theta\cos\theta + \left(\frac{\bar{\beta}}{\bar{\alpha}}\right)^2\frac{\sin^3\theta}{\cos j} \tag{4d}$$

$$\begin{aligned} K = {} & \left[\frac{\bar{\alpha}\bar{\beta}\cos\theta}{\left(\bar{\alpha}^2 - \bar{\beta}^2\right)} - \frac{2\bar{\alpha}^2 + \bar{\beta}^2}{2\left(\bar{\alpha}^2 - \bar{\beta}^2\right)\cos j}\right]\sin^3\theta \\ & + \frac{\bar{\beta}^2}{2\left(\bar{\alpha}^2 - \bar{\beta}^2\right)\cos j}\sin^5\theta \\ & + \left[\frac{\bar{\alpha}^2}{2\left(\bar{\alpha}^2 - \bar{\beta}^2\right)\cos j} - \frac{\bar{\alpha}\bar{\beta}\cos\theta}{2\left(\bar{\alpha}^2 - \bar{\beta}^2\right)}\right]\sin\theta \end{aligned} \tag{4e}$$

$$\begin{aligned} L = {} & \left[-\frac{\bar{\alpha}\bar{\beta}\cos\theta}{\left(\bar{\alpha}^2 - \bar{\beta}^2\right)} + \frac{\bar{\alpha}^2}{\left(\bar{\alpha}^2 - \bar{\beta}^2\right)\cos j}\right]\sin^3\theta \\ & - \frac{\bar{\beta}^2}{\left(\bar{\alpha}^2 - \bar{\beta}^2\right)\cos j}\sin^5\theta. \end{aligned} \tag{4f}$$

Moreover, r_α, r_β, r_ρ, r_ε, and r_δ denote the reflectivities related to the P-wave velocity α, S-wave velocity β, density ρ, and anisotropy parameters ε and δ, respectively

$$r_\alpha = \frac{\Delta\alpha}{\bar{\alpha}}, \quad r_\beta = \frac{\Delta\beta}{\bar{\beta}}, \;\; r_\rho = \frac{\Delta\rho}{\bar{\rho}}, \;\; r_\varepsilon = \Delta\varepsilon, \;\; r_\delta = \Delta\delta \tag{5}$$

where $\bar{\alpha}$, $\bar{\beta}$, and $\bar{\rho}$ denote the averages across the interface, and $\Delta\alpha$, $\Delta\beta$, $\Delta\rho$, $\Delta\varepsilon$, and $\Delta\delta$ are the contrasts between the properties of the upper and lower media. The reflection coefficient of the ith layer and jth incidence angle can be expressed as

$$R\left(t_i, \theta_j\right) = \mathbf{S}\cdot\mathbf{m}, \quad \mathbf{m} = \left[r_\alpha(t_i), r_\beta(t_i), r_\rho(t_i), r_\varepsilon(t_i), r_\delta(t_i)\right]^{\mathrm{T}}. \tag{6}$$

For the PP and PS wave modes, we have

$$\mathbf{S}_{\mathrm{PP}} = \left[A\left(t_i, \theta_j\right), B\left(t_i, \theta_j\right), C\left(t_i, \theta_j\right), D\left(t_i, \theta_j\right), E\left(t_i, \theta_j\right)\right] \tag{7}$$

$$\mathbf{S}_{\mathrm{PS}} = \left[F\left(t_i, \theta_j\right), G\left(t_i, \theta_j\right), H\left(t_i, \theta_j\right), K\left(t_i, \theta_j\right), L\left(t_i, \theta_j\right)\right] \tag{8}$$

which can be computed by (4). Convolving the reflection coefficients with wavelets, we obtain the synthetic seismic data

$$\mathbf{d}_{\mathrm{PP}} = \mathbf{W}_{\mathrm{PP}}\mathbf{R}_{\mathrm{PP}}, \quad \mathbf{d}_{\mathrm{PS}} = \mathbf{W}_{\mathrm{PS}}\mathbf{R}_{\mathrm{PS}} \tag{9}$$

where $\mathbf{W}_{\mathrm{PP}}$ and $\mathbf{W}_{\mathrm{PS}}$ denote the wavelet matrices extracted from the PP and PS data, respectively. Thus, we define

$$\mathbf{G}_{\mathrm{PP}} = \mathbf{W}_{\mathrm{PP}}\mathbf{S}_{\mathrm{PP}}, \quad \mathbf{G}_{\mathrm{PS}} = \mathbf{W}_{\mathrm{PS}}\mathbf{S}_{\mathrm{PS}}. \tag{10}$$

Then, the forward modeling of VTI media can be expressed as a linear problem related to the model vector $\mathbf{m}$ as

$$\mathbf{d}_{\mathrm{PP}} = \mathbf{G}_{\mathrm{PP}}\mathbf{m} = \mathbf{W}_{\mathrm{PP}}\mathbf{S}_{\mathrm{PP}}\mathbf{m}, \quad \mathbf{d}_{\mathrm{PS}} = \mathbf{G}_{\mathrm{PS}}\mathbf{m} = \mathbf{W}_{\mathrm{PS}}\mathbf{S}_{\mathrm{PS}}\mathbf{m}. \tag{11}$$

B. Basis Pursuit Decomposition

A reflectivity series can be represented as a weighted sum of impulse pairs [15]. In the basis pursuit method, each pair of reflectors $\Gamma_1\boldsymbol{\delta}(t)$ and $\Gamma_2\boldsymbol{\delta}(t + i\Delta t)$ can be represented into an odd pair $\mathbf{r}_{\mathrm{o}}$ and an even one $\mathbf{r}_{\mathrm{e}}$ using dipole decomposition

$$\Gamma_1\boldsymbol{\delta}(t) + \Gamma_2\boldsymbol{\delta}(t + i\Delta t) = \mathbf{r}_{\mathrm{o}}\mathbf{m}_{\mathrm{o}} + \mathbf{r}_{\mathrm{e}}\mathbf{m}_{\mathrm{e}} \tag{12}$$

where $\mathbf{m}_{\mathrm{e}}$ and $\mathbf{m}_{\mathrm{o}}$ are the coefficients corresponding to $\mathbf{r}_{\mathrm{o}}$ and $\mathbf{r}_{\mathrm{e}}$, respectively. The odd and even pairs can be computed as

$$\mathbf{r}_{\mathrm{o}} = \boldsymbol{\delta}(t) - \boldsymbol{\delta}(t + i\Delta t), \quad \mathbf{r}_{\mathrm{e}} = \boldsymbol{\delta}(t) + \boldsymbol{\delta}(t + i\Delta t). \tag{13}$$

One can shift the pairs of the whole trace with time interval $k\Delta t$ to obtain the reflectivity series

$$\begin{aligned} \mathbf{r}(t) = \sum_{i=1}^{N}\sum_{j=1}^{M}\big(&\mathbf{m}_{\mathrm{o},i,j}(t, \Delta t)\mathbf{r}_{\mathrm{o},i,j}(t, \Delta t) \\ &+ \mathbf{m}_{\mathrm{e},i,j}(t, \Delta t)\mathbf{r}_{\mathrm{e},i,j}(t, \Delta t)\big) \end{aligned} \tag{14}$$

where

$$\mathbf{r}_{\mathrm{o},i,j}(t, \Delta t) = \boldsymbol{\delta}(t - j\Delta t) - \boldsymbol{\delta}(t + i\Delta t - j\Delta t) \tag{15}$$

$$\mathbf{r}_{\mathrm{e},i,j}(t, \Delta t) = \boldsymbol{\delta}(t - j\Delta t) - \boldsymbol{\delta}(t + i\Delta t - j\Delta t). \tag{16}$$

Similarly, we can decompose the reflectivities as

$$\begin{aligned} \begin{bmatrix} \mathbf{r}_\alpha \\ \mathbf{r}_\beta \\ \mathbf{r}_\rho \\ \mathbf{r}_\delta \\ \mathbf{r}_\varepsilon \end{bmatrix} = {} & \begin{bmatrix} \mathbf{r}_{\mathrm{o}} & \mathbf{r}_{\mathrm{e}} & & & & \cdots & & & & 0 \\ & & \mathbf{r}_{\mathrm{o}} & \mathbf{r}_{\mathrm{e}} & & & & \iddots & & \\ \vdots & & & & \mathbf{r}_{\mathrm{o}} & \mathbf{r}_{\mathrm{e}} & & & & \vdots \\ & & \iddots & & & & \mathbf{r}_{\mathrm{o}} & \mathbf{r}_{\mathrm{e}} & & \\ 0 & & & & \cdots & & & & \mathbf{r}_{\mathrm{o}} & \mathbf{r}_{\mathrm{e}} \end{bmatrix} \\ & \cdot\big[\mathbf{m}_{\mathrm{o},\alpha}, \mathbf{m}_{\mathrm{e},\alpha}, \mathbf{m}_{\mathrm{o},\beta}, \mathbf{m}_{\mathrm{e},\beta}, \mathbf{m}_{\mathrm{o},\rho}, \mathbf{m}_{\mathrm{e},\rho}, \mathbf{m}_{\mathrm{o},\delta}, \mathbf{m}_{\mathrm{e},\delta}, \\ & \quad \mathbf{m}_{\mathrm{o},\varepsilon}, \mathbf{m}_{\mathrm{e},\varepsilon}\big]^{\mathrm{T}}. \end{aligned} \tag{17}$$

Then, (11) can be rewritten as

$$\begin{aligned} \mathbf{d} = \mathbf{W}\cdot\mathbf{S} & \begin{bmatrix} \mathbf{r}_{\mathrm{o}} & \mathbf{r}_{\mathrm{e}} & & & & \cdots & & & & 0 \\ & & \mathbf{r}_{\mathrm{o}} & \mathbf{r}_{\mathrm{e}} & & & & \iddots & & \\ \vdots & & & & \mathbf{r}_{\mathrm{o}} & \mathbf{r}_{\mathrm{e}} & & & & \vdots \\ & & \iddots & & & & \mathbf{r}_{\mathrm{o}} & \mathbf{r}_{\mathrm{e}} & & \\ 0 & & & & \cdots & & & & \mathbf{r}_{\mathrm{o}} & \mathbf{r}_{\mathrm{e}} \end{bmatrix} \\ & \cdot\big[\mathbf{m}_{\mathrm{o},\alpha}, \mathbf{m}_{\mathrm{e},\alpha}, \mathbf{m}_{\mathrm{o},\beta}, \mathbf{m}_{\mathrm{e},\beta}, \mathbf{m}_{\mathrm{o},\rho}, \mathbf{m}_{\mathrm{e},\rho}, \mathbf{m}_{\mathrm{o},\delta}, \mathbf{m}_{\mathrm{e},\delta}, \\ & \quad \mathbf{m}_{\mathrm{o},\varepsilon}, \mathbf{m}_{\mathrm{e},\varepsilon}\big]^{\mathrm{T}}. \end{aligned} \tag{18}$$

C. Anisotropic Inversion With the L_1–L_2-Norm Regularization

Since geophysical inverse problems are always ill-posed, a regularization technique is commonly used to solve the issue. The regularization term is an important factor of the objective function and greatly affects the results. There are many kinds of prior distributions which can be exploited. The expressions of a two-point vector (x_1, x_2) are

$$\begin{aligned} L_2\text{-norm} &= \left(|x_1|^2 + |x_2|^2\right)^{\frac{1}{2}}, \quad L_{\mathrm{Cauchy}}\text{-norm} \\ &= \ln\left(x_1^2 + 1\right) + \ln\left(x_2^2 + 1\right) \end{aligned} \tag{19a}$$

$$\begin{aligned} L_1\text{-norm} &= |x_1| + |x_2|, \quad L_1 - L_2\text{-norm} \\ &= |x_1| + |x_2| - a\left(|x_1|^2 + |x_2|^2\right)^{\frac{1}{2}} \end{aligned} \tag{19b}$$

$$L_P\text{-norm} = \left(|x_1|^P + |x_2|^P\right)^{\frac{1}{P}}, \quad 0 < P < 1 \tag{19c}$$

$$L_0\text{-norm} = \begin{cases} 0, & (x_1, x_2) = 0 \\ 2, & x_1x_2 \neq 0 \\ 1, & \text{else} \end{cases} \tag{19d}$$

where a is a scale coefficient, which can be used to adjust the sparseness of the L_1–L_2-norm.

We show the distribution properties of these norms for a vector with two elements in Fig. 1, according to (19). For an absolutely sparse two-element vector, at least one of the elements should be zero. In this case, the solution is mainly confined at the coordinate axis as can be seen in Fig. 1(f). Therefore, the L_0-norm [Fig. 1(f)] has the sparsest distribution among all these norms. The closer the property of the norm

Authorized licensed use limited to: Konya Teknik Universitesi. Downloaded on May 25,2021 at 23:14:15 UTC from IEEE Xplore. Restrictions apply.

This article has been accepted for inclusion in a future issue of this journal. Content is final as presented, with the exception of pagination.

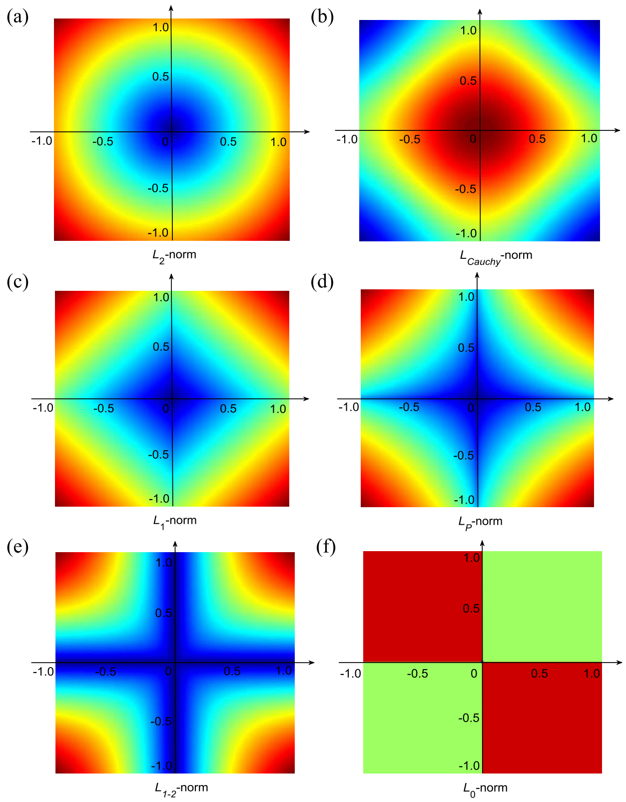

Fig. 1. Distribution properties of different regularization terms. The different norms are (a) L_2, (b) L_{Cauchy}, (c) L_1, (d) L_P, (e) L_1–L_2, and (f) L_0.

is to that of L_0, the sparser distribution it has. The smooth norm, L_2, in Fig. 1(a), in contrast, has a different behavior. Compared with L_1, L_P, and L_{Cauchy} ones, the L_1–L_2 norm shows a better performance, as we shall see.

In the conventional BPI, the L_1-norm is used as regularization constraint, and the objective function is

$$J(\mathbf{m}) = \left\{\kappa\|\mathbf{G}_{\mathrm{PP}}\mathbf{m}-\mathbf{d}_{\mathrm{PP}}\|_2^2+(1-\kappa)\|\mathbf{G}_{\mathrm{PS}}\mathbf{m}-\mathbf{d}_{\mathrm{PS}}\|_2^2+\lambda\|\mathbf{m}\|_1\right\} \tag{20}$$

where λ is the regularization weight, which balances the data misfit and regularization terms, and κ is a weight factor for the type of data. This method, used to improve the vertical resolution, should take into account the sparser constraint. The L_0-norm has the best performance in sparsity, but it is a NP-hard problem (a nondeterministic polynomial problem whose solution is difficult to find and verify). Therefore, we introduce the L_1–L_2 norm as regulation constraint, with the objective function

$$J(\mathbf{m}) = \kappa\|\mathbf{G}_{\mathrm{PP}}\mathbf{m}-\mathbf{d}_{\mathrm{PP}}\|_2^2+(1-\kappa)\|\mathbf{G}_{\mathrm{PS}}\mathbf{m}-\mathbf{d}_{\mathrm{PS}}\|_2^2 + \lambda(\|\mathbf{m}\|_1 - a\|\mathbf{m}\|_2). \tag{21}$$

Since this function is nonconvex, it cannot be solved with the conventional optimization. Then, the ADMM algorithm is adopted. We introduce an auxiliary variable $\mathbf{z}$ which is subject to $\mathbf{m}-\mathbf{z}=\mathbf{0}$, so that nonconvex function (21) is decomposed into two convex subproblems

$$\arg\min\{f(\mathbf{m})+g(\mathbf{z})\} \tag{22}$$

where $f(\mathbf{m}) = \kappa\|\mathbf{G}_{\mathrm{PP}}\mathbf{m}-\mathbf{d}_{\mathrm{PP}}\|_2^2+(1-\kappa)\|\mathbf{G}_{\mathrm{PS}}\mathbf{m}-\mathbf{d}_{\mathrm{PS}}\|_2^2 - \lambda a\|\mathbf{m}\|_2$ and $g(\mathbf{z}) = \lambda\|\mathbf{z}\|_1$. The process for solving (22) is as follows. First, we update $\mathbf{x}$ by minimizing the $\mathbf{x}$-related

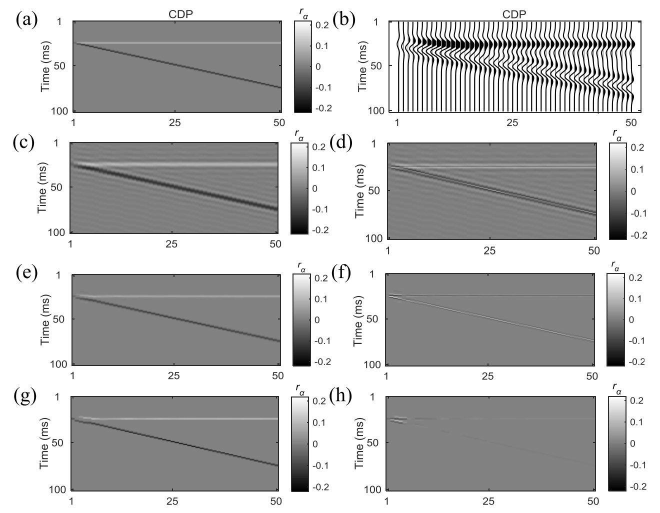

Fig. 2. Inverted r_α of a wedge model with (c) and (d) JRI and (e)–(h) JBPAI without noise. (a) True r_α. (b) Synthetic poststack profile. (c) r_α by L_2-based JRI. (d) Residuals between (a) and (c). (e) JBPAI with the L_1-norm. (f) Residuals between (a) and (e). (g) JBPAI with the L_1–L_2-norm. (h) Residuals between (a) and (g).

augmented Lagrangian function

$$\mathbf{m}^{k+1} = \arg\min_{m} L_\rho\left(\mathbf{m}, \mathbf{z}^k, \mathbf{y}^k\right). \tag{23}$$

Second, $\mathbf{z}$ is updated by solving

$$\mathbf{z}^{k+1} = \arg\min_{z} L_\rho\left(\mathbf{m}^{k+1}, \mathbf{z}, \mathbf{y}^k\right). \tag{24}$$

Then, we update the Lagrangian multiplier

$$\mathbf{y}^{k+1} = \mathbf{y}^k + \mu\left(\mathbf{m}^{k+1} - \mathbf{y}^{k+1}\right) \tag{25}$$

where μ is a penalty coefficient.

III. Synthetic Data Test

A. Wedge Model Inversion

A benchmark wedge model is used to test the validity of the L_1–L_2-based BPI. The model tests the ability of the inversion to handle thin layers. The synthetic gathers are obtained by convolving the reflection coefficients, calculated with the Rüger approximations in (1)–(8), with a Ricker wavelet, and the corresponding poststack profile is shown in Fig. 2(b). We compare algorithms, namely, the conventional joint Rüger-approximation-based inversion (JRI) with the L_2-norm [Fig. 2(c)] and the joint basis pursuit anisotropic inversion (JBPAI) with the L_1 [Fig. 2(e)] and L_1–L_2 norms [Fig. 2(g)] in the absence of noise. The residuals between the inverted results and the true reflectivities are shown in Fig. 2(d) (JRI), Fig. 2(f) (JBPAI with L_1-norm), and Fig. 2(h) (JBPAI with L_1–L_2-norm). The aim of the noise-free test is to highlight the resolution of the method, and we only show the inverted r_α for brevity. Compared with JBPAI, the reflectivities of the JRI with the L_2-norm are fuzzy, which are not enough to describe the interfaces and distinguish the top and bottom of thin layers. The results of L_1–L_2-based JBPAI have a higher resolution than those of the L_1 inversion (sparser inverted reflectivity), which can be better seen from the residual profiles [Fig. 2(f) and (h)].

Authorized licensed use limited to: Konya Teknik Universitesi. Downloaded on May 25,2021 at 23:14:15 UTC from IEEE Xplore. Restrictions apply.

This article has been accepted for inclusion in a future issue of this journal. Content is final as presented, with the exception of pagination.

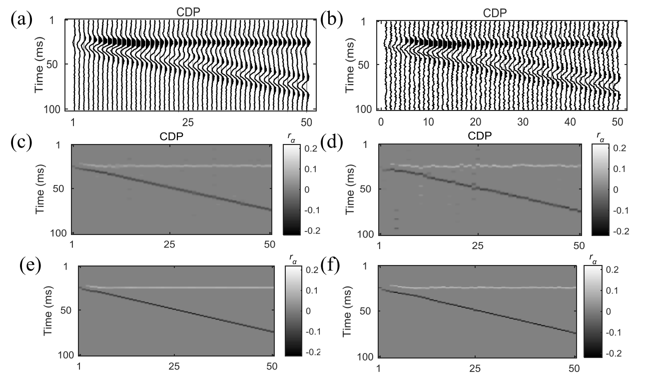

Fig. 3. Synthetic data with (a) SNR = 5 and (b) SNR = 2. Inverted r_α of (c) and (d) L_1-based and (e) and (f) L_1–L_2-based JBPAI in case of (c) and (e) SNR = 5 and (d) and (f) SNR = 2.

B. Noise Test

We add a certain amount of noise to the synthetics of the wedge model. Fig. 3 shows the inverted reflectivities using the L_1- [Fig. 3(c) and (d)] and L_1–L_2-norms [Fig. 3(e) and (f)] (JBPAI), which are obtained with signal-to-noise ratios (SNRs) of 5 [Fig. 3(c) and (e)] and 2 [Fig. 3(d) and (f)]. Fig. 3(c) and (d) shows that the noise interference causes outliers in the L_1 results. Although the gathers with SNR = 5 give an acceptable r_α, the L_1-based algorithm cannot handle interferences. In contrast, the results with the L_1–L_2 norm show a higher resolution, better lateral continuity, and stability.

C. Well Model Test

The well-log curves are used to test the effectiveness for all the inverted properties, namely, P-wave velocity α, S-wave velocity β, density ρ, and anisotropic parameters ε and δ. The input PP and PS gathers are computed with Rüger's simplified equations, and two methods, the L_2-based JRI [Fig. 4(a)] and the L_1–L_2-based JBPAI [Fig. 4(b)], are adopted (noise-free case). The JBPAI algorithm achieves higher resolution results than the JRI one. Then, the first is tested with SNR = 5 [Fig. 4(c)] and SNR = 2 [Fig. 4(d)], where we can see that the performance is satisfactory. The root-mean-square errors (RMSEs) between the true curves and the inverted properties with SNR = 5 are 2.467 (α), 2.485 (β), 0.528 (ρ), 10.457 (ε), and 12.265 (δ). Although accuracy decreases with noise [see Fig. 4(c) and (d)], the results for SNR = 2 are still acceptable, since the RMSEs are 3.213 (α), 3.916 (β), 0.893 (ρ), 16.119 (ε), and 18.612 (δ). The analysis shows that JBPAI with L_1–L_2-norm is stable and reliable with high noise levels.

IV. Field Data Example

The proposed L_1–L_2-based JBPAI algorithm is applied to the PP and PS seismic data from Western China and also compared with the L_2-based JRI. The target section is a set of shale layers with a relatively stable geological structure. The data consist of 60 gathers with incident angles ranging from 5° to 35° (PP) and 5° to 30° (PS), respectively. Before implementing the inversion, the PS gathers have to be compressed into the PP time domain, a process that can greatly affect the inversion results. Here, we adopt dynamic time warping [28] to perform this procedure. Then, the angle gathers are processed into partial stacked sections to suppress random noise. Since the anisotropy parameters cannot be measured directly in wells, an effective rock-physics-based estimation method is adopted to predict these two parameters at the well position [29]. Fig. 5 shows the results of the five parameters inverted by the conventional JRI with the L_2-norm and the proposed JBPAI with the L_1–L_2-norm. These profiles show that compared with the conventional method, JBPAI can effectively improve the vertical resolution. Near the borehole (common depth point (CDP) 31), the JBPAI achieves relatively reasonable RMSEs for α (5.93), β (6.64), and ρ (1.31), but unacceptable values for ε (20.94) and δ (23.06). To improve the accuracy of the anisotropy parameters, large-angle gathers and a more accurate forward modeling need to be considered in a future study.

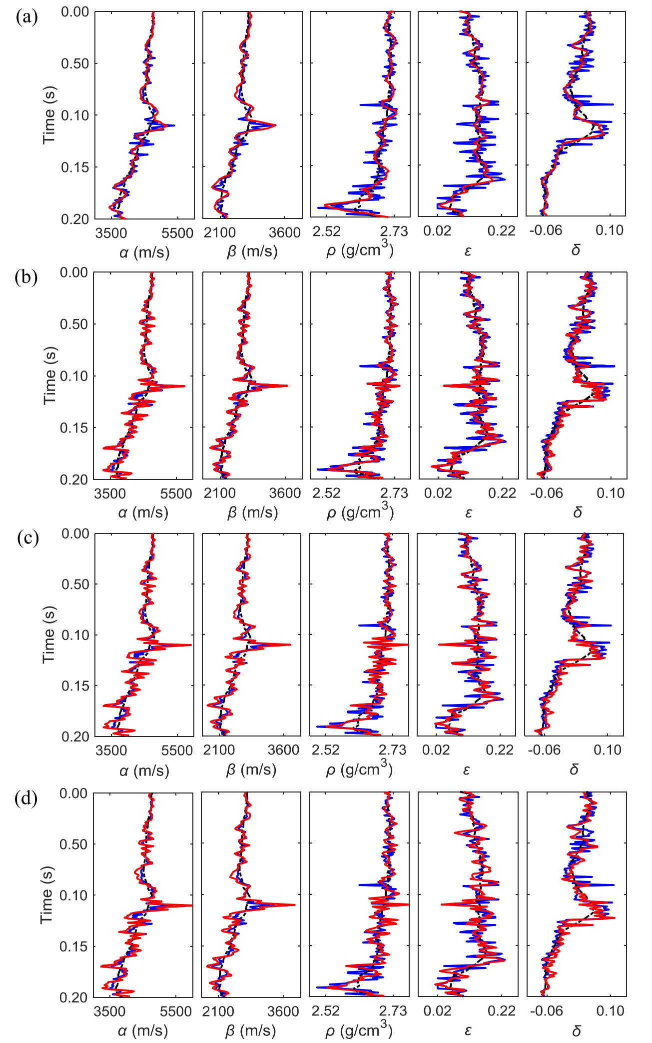

Fig. 4. Inverted properties of the well model with (a) JRI and (b)–(d) JBPAI algorithms (a) and (b) without and with noise: (c) SNR = 5 and (d) SNR = 2. The blue-solid, black-dotted, and red-solid curves represent the true logs, initial models, and inversion results, respectively.

V. Conclusion

We have proposed a JBPAI method for VTI media based on the Rüger approximation. Instead of the L_1-norm, a commonly used sparse constraint, we use the L_1–L_2-norm to improve the resolution and stability of the algorithm. Tests with wedge model and with well-log profiles show the method can achieve high resolution, even in the presence of noise. Application to a set of multicomponent data of a shale reservoir illustrates the performance of inversion.

L_1–L_2 is introduced into the proposed JBPAI, which does not mean that this norm is specifically more suitable for anisotropic conditions. This L_1–L_2-based BPI scheme, in fact, is applicable to both isotropic and anisotropic conditions when high-resolution results are desired. We aim to improve the

Authorized licensed use limited to: Konya Teknik Universitesi. Downloaded on May 25,2021 at 23:14:15 UTC from IEEE Xplore. Restrictions apply.

This article has been accepted for inclusion in a future issue of this journal. Content is final as presented, with the exception of pagination.

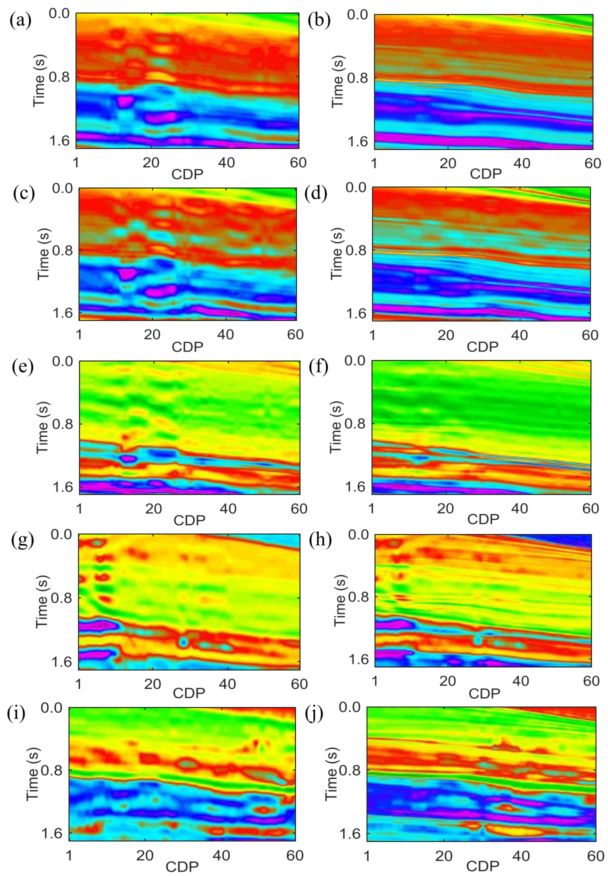

Fig. 5. Inverted 2-D profiles by (a), (c), (e), (g), and (i) JRI with the L_2-norm and (b), (d), (f), (h), and (j) JBPAI with the L_1–L_2-norm, including (a) and (b) P-wave velocity α, (c) and (d) S-wave velocity β, (e) and (f) density ρ, and anisotropy parameters, (g) and (h) ε, and (i) and (j) δ.

vertical resolution of the anisotropic inversion here, but not the inversion accuracy. Similar to the conventional anisotropic inversion, the method is limited by the relatively low accuracy of the simplified forward operator in the medium-to-large angle range, where the seismic gathers contain important information on the anisotropy parameters. Future studies will intend to improve the accuracy by introducing a suitable forward operator and making use of large-angle gathers. Besides, it should be noted that the L_1–L_2-norm, a combination of L_1 and L_2, often results in a balanced result rather than a better result. One can adjust the scale coefficient a to achieve the desired results.

Acknowledgment

The authors would like to thank G. Huang and Y. Chen for their help and also like to thank the Associate Editor and the anonymous reviewers for their helpful comments.

References

[1] G. Huang, X. Chen, C. Luo, M. Bai, and Y. Chen, "Time-lapse seismic difference-and-joint prestack AVA inversion," *IEEE Trans. Geosci. Remote Sens.*, early access, Dec. 14, 2020, doi: 10.1109/TGRS.2020.3038762.

[2] C. Luo, J. Ba, J. M. Carcione, G. Huang, and Q. Guo, "Joint PP and PS pre-stack seismic inversion for stratified models based on the propagator matrix forward engine," *Surv. Geophys.*, vol. 41, no. 5, pp. 987–1028, Sep. 2020.

[3] G. Huang, X. Chen, C. Luo, and Y. Chen, "Geological structure-guided initial model building for prestack AVO/AVA inversion," *IEEE Trans. Geosci. Remote Sens.*, vol. 59, no. 2, pp. 1784–1793, Feb. 2021.

[4] C. Luo, G. Huang, X. Chen, and Y. Chen, "Registration-free multicomponent joint AVA inversion using optimal transport," *IEEE Trans. Geosci. Remote Sens.*, early access, Mar. 18, 2021, doi: 10.1109/TGRS.2021.3063271.

[5] L. Perozzi, E. Gloaguen, B. Giroux, and K. Holliger, "A stochastic inversion workflow for monitoring the distribution of CO_2 injected into deep saline aquifers," *Comput. Geosci.*, vol. 20, no. 6, pp. 1287–1300, Dec. 2016.

[6] K. Li, X. Yin, and Z. Zhao, "Bayesian seismic multi-scale inversion in complex Laplace mixed domains," *Petroleum Sci.*, vol. 14, pp. 697–710, Dec. 2017.

[7] Q. Guo, H. Zhang, F. Han, and Z. Shang, "Prestack seismic inversion based on anisotropic Markov random field," *IEEE Trans. Geosci. Remote Sens.*, vol. 56, no. 2, pp. 1069–1079, Feb. 2018.

[8] W. Alemie and M. D. Sacchi, "High-resolution three-term AVO inversion by means of a trivariate cauchy probability distribution," *Geophysics*, vol. 76, no. 3, pp. R43–R55, May 2011.

[9] C. Luo, X. Li, and G. Huang, "Pre-stack AVA inversion by using propagator matrix forward modeling," *Pure Appl. Geophys.*, vol. 176, no. 10, pp. 4445–4476, Oct. 2019.

[10] Y.-K. Tian, H. Zhou, H.-M. Chen, Y.-M. Zou, and S.-J. Guan, "Bayesian prestack seismic inversion with a self-adaptive huber-Markov random-field edge protection scheme," *Appl. Geophys.*, vol. 10, no. 4, pp. 453–460, Dec. 2013.

[11] C. Li and F. Zhang, "Amplitude-versus-angle inversion based on the L_1-norm-based likelihood function and the total variation regularization constraint," *Geophysics*, vol. 82, no. 3, pp. R173–R182, 2017.

[12] G. Huang *et al.*, "The slope-attribute-regularized high-resolution prestack seismic inversion," *Surv. Geophys.*, vol. 4, pp. 1–41, Mar. 2021, doi: 10.1007/s10712-021-09636-6.

[13] Q. Guo, H. Zhang, H. Cao, W. Xiao, and F. Han, "Hybrid seismic inversion based on multi-order anisotropic Markov random field," *IEEE Trans. Geosci. Remote Sens.*, vol. 58, no. 1, pp. 407–420, Jan. 2019.

[14] Q. Guo, J. Ba, and C. Luo, "Prestack seismic inversion with data-driven MRF-based regularization," *IEEE Trans. Geosci. Remote Sens.*, early access, Nov. 6, 2020, doi: 10.1109/TGRS.2020.3019715.

[15] R. Zhang and J. Castagna, "Seismic sparse-layer reflectivity inversion using basis pursuit decomposition," *Geophysics*, vol. 76, no. 6, pp. R147–R158, Nov. 2011.

[16] R. Zhang, M. K. Sen, and S. Srinivasan, "A prestack basis pursuit seismic inversion," *Geophysics*, vol. 78, no. 1, pp. R1–R11, Jan. 2013.

[17] P. Ding, D. Wang, G. Di, and X. Li, "Investigation of the effects of fracture orientation and saturation on the Vp/Vs ratio and their implications," *Rock Mech. Rock Eng.*, vol. 52, no. 9, pp. 3293–3304, Sep. 2019.

[18] C. Luo, J. Ba, J. M. Carcione, G. Huang, and Q. Guo, "Joint PP and PS pre-stack AVA inversion for VTI medium based on the exact graebner equation," *J. Petroleum Sci. Eng.*, vol. 194, Nov. 2020, Art. no. 107416.

[19] F. Zhang, T. Zhang, and X. Li, "Seismic amplitude inversion for the transversely isotropic media with vertical axis of symmetry," *Geophys. Prospecting*, vol. 67, no. 9, pp. 2368–2385, Nov. 2019.

[20] M. Graebner, "Plane-wave reflection and transmission coefficients for a transversely isotropic solid," *Geophysics*, vol. 57, no. 11, pp. 1512–1519, Nov. 1992.

[21] M. Schoenberg and J. Protazio, "'Zoeppritz' rationalized and generalized to anisotropy," *J. Seismic Explor.*, vol. 1, pp. 125–144, 1992.

[22] J. Carcione, *Wave Fields in Real Media Theory and Numerical Simulation of Wave Propagation in Anisotropic, Anelastic, Porous and Electromagnetic Media*. Amsterdam, The Netherlands: Elsevier, 2014.

[23] A. Ráger, "Variation of P-wave reflectivity with offset and azimuth in anisotropic media," *Geophysics*, vol. 63, no. 3, pp. 935–947, May 1998.

[24] J. Lu, Y. Wang, J. Chen, and Y. An, "Joint anisotropic amplitude variation with offset inversion of PP and PS seismic data," *Geophysics*, vol. 83, no. 2, pp. N31–N50, Mar. 2018.

[25] Y. Lou and M. Yan, "Fast L_1–L_2 minimization via a proximal operator," *J. Sci. Comput.*, vol. 74, no. 2, pp. 767–785, Feb. 2018.

[26] L. Wang *et al.*, "Three-parameter prestack seismic inversion based on L_{1-2} minimization," *Geophysics*, vol. 84, no. 5, pp. R753–R766, Sep. 2019.

[27] P. F. Daley and F. Hron, "Reflection and transmission coefficients for transversely isotropic media," *Bull. Seismol. Soc. Amer.*, vol. 67, no. 3, pp. 661–675, 1977.

[28] D. Hale, "A method for estimating apparent displacement vectors from time-lapse seismic images," *Geophysics*, vol. 74, no. 5, pp. V99–V107, Sep. 2009.

[29] F. Zhang, "Estimation of anisotropy parameters for shales based on an improved rock physics model, Part 2: Case study," *J. Geophys. Eng.*, vol. 14, no. 2, pp. 238–254, Mar. 2017.

Authorized licensed use limited to: Konya Teknik Universitesi. Downloaded on May 25,2021 at 23:14:15 UTC from IEEE Xplore. Restrictions apply.